Impact of the Level of Homogenization in 3D Thermal Simulation on the Internal Temperature Distribution of Li-Ion Battery Cells

Oliver Queisser, Lisa Cloos, Friederike Boehm, Dieter Oehler, and Thomas Wetzel*

Temperature is an important factor for an optimal battery performance. To gain knowledge about the internal temperature distribution in a battery, many thermal simulation studies are performed. Among other factors, they differ in the level of homogenization (LoH) of the geometry, which directly influences the computing time. However, the effects of different LoH, in particular of the cell layers, on the modeling and prediction quality of the temperature field are scarcely investigated. This work discusses the effect of different LoH of the cell stack on a numerical 3D thermal battery model for different thermal management strategies. A new approach of reducing the number of cell layers of the pouch cell geometry while keeping their volumetric proportions constant is proposed. It is clearly shown that the LoH has a large impact on the thermal transport paths, especially through the current collectors and tabs, and therefore on the predicted internal temperature distribution. In addition, the effect of the LoH differs for different thermal management strategies, because they affect the heat transport paths as well.

1. Introduction

Many mobile applications used in daily life require Li-ion batteries. The performance and degradation[1,2] behavior of these batteries depend, among other factors, on the internal temperature.[3] It is affected by the heat generated from irreversible reactions and reversible processes inside the cell[4] and the applied boundary conditions through thermal management strategies.[5,6] For example, in some electric vehicles, the cells are actively cooled to achieve an optimal application temperature between 20 and 40 °C.[7] Apart from the cooling strategy, the battery format can help to reduce the peak temperature inside the cell. Li-ion batteries in pouch format with side cooling have the

advantage of the lowest temperature rise in comparison with other formats.[8]

Different cooling strategies again affect the internal temperature field in various specific ways. Liebig et al.[9] investigated the interaction of these cooling strategies with heat transport paths using a coupled electrochemical–thermal model. They found that higher temperature levels are reached for natural and forced convection than for cooling scenarios, where heat conduction is dominant. Zhao et al.[5] assess the differences between conductive tab and surface cooling with their 2D electrothermal model. The cell stack geometry of the thermal model consists of nodes representing unit cells (current collectors, anode and cathode coatings, and separator) mapped as an equivalent circuit network model. The tabs are resolved as well. According to their results, surface cooling leads to a lower average temperature with a higher temperature gradient, whereas tab cooling shows exactly the opposite. Hunt et al.[6] experimentally found a stronger capacity loss for surface cooling than tab cooling and attributed it to larger thermal gradients perpendicular to the cell stack, resulting from surface cooling. Guo et al.[10] also found larger thermal gradients perpendicular to the cell stacks than in plane with their 3D thermal model in a 150 °C "oven test", which they attributed to the lower effective thermal conductivity in this direction.

Thus, the internal temperature field is not only of high relevance but also difficult to measure.[11,12] Thermal simulations allow a detailed insight into the temperature field. There are two main approaches of thermal modeling: 1) equivalent circuit network models, as presented by Zhao et al.[5] and 2) physical models based on the transient heat equation including a heat source.[4] With both approaches, there is a trade-off between quality and computational cost. To reduce the computing time, simplifications have to be made and evaluated. Typical approaches are a reduction of the dimension or a homogenization of the geometry.

The homogenization of the geometry can be divided into two parts—the external components such as tabs, connectors, and housing, and the inner cell stack or jelly roll structure. Cui et al.[13] performed a 3D thermal simulation on a hard case cell with a homogenized cell stack. If the internal temperature field is of interest, they suggest resolving the housing and the outer separator as a thermal contact resistance. In comparison with the results of a completely homogenized battery geometry,

O. Queisser, L. Cloos, F. Boehm, D. Oehler, Prof. T. Wetzel
Karlsruhe Institute of Technology
Kaiserstr. 12, 76131 Karlsruhe, Germany
E-mail: oliver.queisser@kit.edu

The ORCID identification number(s) for the author(s) of this article can be found under https://doi.org/10.1002/ente.202000915.

the temperature deviates by a root-mean square of 1.2 K. Chen et al.[14] show with their thermal 3D model, that the hard case is an important heat transport path, whereas the contact layer, which is located between case and cell stack, is thermally resistant. Equivalent to the housing of prismatic cells, the resolution of cell tabs in a pouch cell is important for thermal simulation. Goutam et al.[15] presented a 2D electrical model coupled into a 3D thermal model and evaluated different simplifications such as cell geometry, dimensionality, and heat-generation rate. Their thermal model resolves the core, casing, and the tabs. They found that the tabs improve heat transport and reduce inhomogeneity in temperature. In addition, they state that a 3D geometry is necessary to map the temperature field accurately, whereas a nonuniform heat-generation rate is not necessary.

The homogenization of the cell structure can be performed "bottom up" or "top down". Asymptotic homogenization of the microscale structures of the electrode coating could be described as a "bottom up" approach. With this approach, Hunt et al.[16] combined an electrochemical model at cell level with a thermal model at unit cell or battery level. A common "top down" approach is the homogenization of the cell stack to one block with anisotropic material properties based on calculations.[17] Chen et al.[14] compare the results of a thermal simulation on a homogenized cell stack to a fully resolved (FR) one. The FR geometry consists of the current collectors, their respective active material layers, and a separator. The heat-generation equation by Bernardi et al.[4] is applied and convection as well as radiation boundary conditions are considered. They conclude that the homogenized model can achieve almost the same results and has a 660 times shorter computing time in their specific case.

Some authors present partially homogenized (PH) approaches. Mei et al.[18] propose a 3D electrochemical–thermal model for three different geometries. The tab is mapped. First, due to the very thin layers of the anode and cathode current collectors, active material coatings and the separator, they propose a magnification of a unit cell to the dimensions of the battery. They compare the geometry of a unit cell and two unit cells to the half of a FR cell stack. They suggest that the temperature distribution of a magnified unit cell is comparable to that of a full-scale model and can reduce the computing time by factor 140. Allu et al.[19] perform a 3D electrochemical–electro–thermal simulation with a heat release term by Bernardi et al.[4] They homogenized the active material layers and separator layer while they mapped the current collectors examining a cylindrical and a pouch cell. For the cylindrical cell, the case was not mapped, whereas in the pouch cell an individual layer was implemented. A convective thermal boundary condition was set in which they varied the heat-transfer coefficient in case of the pouch cell. Based on their results, they stress the importance of the metallic current collectors for thermal transport.

Although most authors agree on the importance of modeling the cell tabs and housing, opinions on the role of current collectors inside the cell structure vary. As current collectors thermally conduct just as well as the cell tabs, further investigation of their impact on heat transport paths is necessary. As different cooling approaches address different heat transport paths, they have to be included in the investigation as well. Although it is important to model the temperature field accurately, a mapping of each layer in the cell stack is highly time consuming. The layers are very thin and therefore the grid must become extremely fine,

resulting in a very high number of degrees of freedom to avoid unfavorable aspect ratios of finite volumes or finite elements. Furthermore, to minimize the increase in computing time, a different PH approach might be necessary.

In this work, a 3D thermal model for a pouch cell geometry and conductive cooling, including one-sided, two-sided, and tab cooling, is presented. Then the effect of different LoH of the geometry on the temperature field is discussed in the following steps. First, the geometry is FR, which is the chosen reference case. Second, it is fully homogenized (FH), as in common practice. In addition, the active material layers and separator layer are homogenized as presented by Allu et al.[19] Then, a new PH approach is presented. The results of the different approaches are compared with the reference case and evaluated by their prediction quality and computing time.

2. Thermal Battery Model

2.1. Thermal Transport

The 3D thermal battery model is based on the transient heat conduction equation in the form of Equation (1), as commonly done in physics-based models. It is solved using the Finite Volume Method (FVM) as implemented in the software OpenFOAM version 6, applying the solver chtMultiRegionFoam.[20]

$$\rho c_{\mathrm{p}} \frac{\partial T}{\partial t} = \nabla \cdot (\bar{\bar{\lambda}} \nabla T) + \dot{Q}_{\mathrm{src}}''' \tag{1}$$

The equation consists of the transient storage term, including the density ρ and the specific heat capacity c_{p}, on the left, as well as the sum of the thermal transport term, containing the thermal conductivity tensor $\bar{\bar{\lambda}}$, and the volumetric heat source $\dot{Q}_{\mathrm{src}}'''$ on the right-hand side. Bernardi et al.[4] have presented the composition of the heat source in battery cells in detail.

In this work, a nondimensionalized temperature as defined in Equation (2) is used. T_{max} represents the maximum temperature of all simulations and T_{min} the corresponding minimum temperature. The result is the dimensionless temperature Θ, whose minimum value is obviously zero and maximum value is one.

$$\Theta = \frac{T - T_{\mathrm{min}}}{T_{\mathrm{max}} - T_{\mathrm{min}}} = \frac{T - T_{\mathrm{min}}}{\Delta T_{\mathrm{max}}} \tag{2}$$

The advantage of the nondimensionalization is the opportunity to make general valid statements about the temperature distribution, independent from specific temperature levels of e.g., the boundary conditions. Equation (3) follows from inserting the dimensionless temperature into the heat equation.

$$\frac{\partial \Theta}{\partial t} = \nabla \cdot \left(\frac{\bar{\bar{\lambda}}}{\rho c_{\mathrm{p}}} \nabla \Theta \right) + \frac{\dot{Q}_{\mathrm{src}}'''}{\rho c_{\mathrm{p}} \Delta T_{\mathrm{max}}} \tag{3}$$

For the actively cooled parts of the battery cell, a Dirichlet boundary condition, given in Equation (4), is applied to the respective surfaces of the geometry. To the rest of the battery geometry an adiabatic boundary condition normal to the surface was applied, which is a specific expression of the Neumann condition (Equation 5).

$$\Theta = \Theta_{\text{Dirichlet}-\text{BC}} \qquad (4)$$

$$-\lambda_{\text{n}} \frac{\partial \Theta}{\partial n} = 0 \qquad (5)$$

2.2. Model Approach

The model was developed for a pouch cell geometry. The cell stack, in which the electrochemical reactions and thus the majority of the heat generation are taking place, is the main part of the battery cell. It is located centrally in the geometry and surrounded by an outer separator shell followed by the pouch foil. At each front side, the cell stack is connected to a tab which is simplified to a T-shape. If the cell stack is simply considered a fully homogeneous block (cf. **Figure 1**), the heat from tabs to stack or vice versa will be transferred over the whole contact area.

However, if any current collector layers are resolved within this model geometry, the tab is only connected to the respective current collector foils. The remaining layers are isolated using a fictional layer with a very low thermal conductivity to reduce the heat flow to approximately zero. Similarly, heat is then only generated in the active material or in the anode and cathode coatings. So, if any current collectors are resolved, the heat release is assumed to be negligible, as done by Liebig et al.[9] However, the integral heat generation in the cell is the same as in the fully homogeneous block.

The homogenization of the general model geometry will now be presented in more detail. The tab, the outer separator, and the pouch foil, respectively casing, are resolved in every simulation case, as it is necessary to increase accuracy.[13,15] The focus of this contribution is on the level of homogenization (LoH) of the cell stack. The most realistic representation of the inner structure of a cell stack on electrode level is to resolve each individual layer (FR model). The unit cell for the aforementioned case is shown in **Figure 2**a. The anode current collector (copper) and cathode
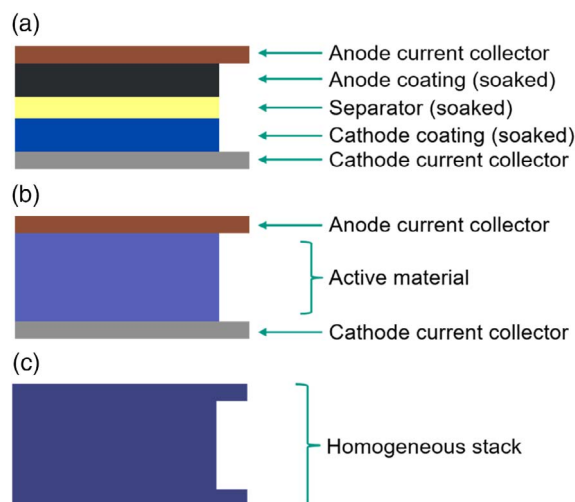
Figure 2. a) FR, b) PH, and c) FH approach of a unit cell.

current collector (light gray), as well as the anode coating (black), cathode coating (cobalt blue), and the separator (yellow) are mapped. This is the selected reference case as it represents the most realistic mapping of the cell geometry. It is the starting point for further simplifications.

Because of the huge number of single layers and their very small thickness compared with the lateral dimensions of the cell, a very fine grid with a lot of very small finite volumes, and therefore large number of degrees of freedom, is necessary to resolve the model without homogenization. This results in a high computing time, which will be discussed for the studies conducted in Section 3.3. Therefore, as already mentioned in Section 1, it is common to fully homogenize the cell stack (FH model)[13,14] and assign effective parameters according to the volumetric fraction for simulation (cf. Section 2.4). In this approach, a PH is
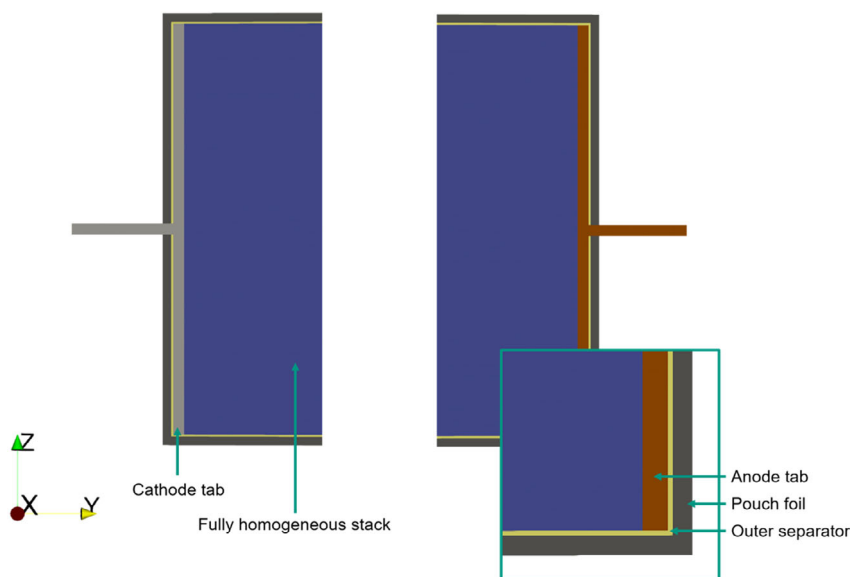
Figure 1. Model geometry with resolved cathode tab (light gray), anode tab (copper), pouch foil (dark gray), outer separator layer (yellow), and FH cell stack (dark blue).

ADVANCED
SCIENCE NEWS
www.advancedsciencenews.com

Energy Technology
Generation, Conversion, Storage, Distribution
www.entechnol.de

realized in two steps. In the first step, the anode and cathode coating as well as the separator are combined to one active material layer (light blue) as shown in Figure 2b. This is similar to the FH approach (dark blue in Figure 2c), yet the current collector foils with their very high thermal conductivity are still resolved. Allu et al.[19] first presented this concept. The thermal material properties are homogenized, respectively. The resulting anisotropic thermal conductivity is in the same order of magnitude as those of the individual layers (cf. Table 2). This approach provides an intermediate path between the FH and the FR approach. After homogenizing the coating layers and the separator layer to an active material layer, the number of layers is still high. Therefore, a second step of homogenization is introduced. The volume fraction of each layer related to the entire cell stack is kept constant, whereas the number of layers is reduced. This means, that the number of layers decreases, whereas the thickness of each layer increases. The resulting geometry for a PH with 8 unit cells and 17 layers in total is shown in **Figure 3**.

2.3. Simulation Studies

In the simulation studies, the FR and FH case as well as multiple PH cases are performed. The FR case consists of 265 layers. When homogenizing the coatings and separator to active material layers, the PH case has 133 layers (PH133). The number of unit cells in FR and PH133 case are the same. In the next step, the number of unit cells is reduced. The cell stack is symmetrical with cathode current collector layers on top and bottom. In the middle is either a cathode current collector or an anode current collector. With that in mind, the cases PH49, PH29, PH17, and PH5 are chosen with the respective amount of layers. As the goal is to reduce computing time, a graded selection toward lesser layers was chosen. The case PH5 has the minimum amount of five layers and one unit cell. The heat-generation rate is evenly applied over the homogenized stack (FH), in the active material (PH), or in the coatings (FR) as described earlier.

In addition to these differently homogenized geometries, different boundary conditions are applied. Three cooling scenarios with the same "coolant" temperature are chosen. Therefore, they all correspond to the dimensionless temperature zero. The first cooling scenario is one-sided cooling of the lower surface of the battery geometry. In the second cooling scenario, a two-sided cooling, the upper surface is additionally controlled. The third scenario represents tab cooling, in which the cooling condition
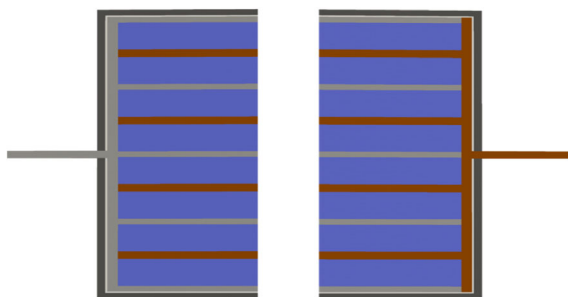
Table 1. Overview of possible settings concerning LoH and cooling strategy as well as available point probes and 2D slices for evaluation.

Level of homogenization	Cooling strategy	Point probe	2D slice in yz-plane
Fully homogenized (FH)	One-sided cooling without heat release (0)	Lower side (A)	FH (i)
Partially homogenized with 5 layers (PH5)	One-sided cooling (1)	Upper side (B)	PH133 (ii)
Partially homogenized with 17 layers (PH17)	Two-sided cooling (2)	Edge (C)	FR (iii)
Partially homogenized with 29 layers (PH29)	Tab cooling (3)	Center (D)	–
Partially homogenized with 49 layers (PH49)	–	–	–
Partially homogenized with 133 layers (PH133)	–	–	–
Fully resolved (FR)	–	–	–

is applied to the surfaces of both tabs. An overview of the different parameters of the simulation cases and the evaluated probes is presented in **Table 1**.

2.4. Parameterization

The following section deals with the thermal parameterization of the individual cell layers depending on the LoH, as mentioned earlier. Both the heat source and thermal material properties are dependent on the state of charge (SOC) and the temperature level.[21] Nevertheless, the mentioned parameters are assumed to be constant in this contribution, because the impact of the LoH in the thermal model is supposed to be investigated without any influence by the dependencies of the electrochemical cell properties. The thermal transport properties of the individual cell layers used for parameterization are listed in **Table 2** at a

Table 2. Thermal transport parameters of the individual cell layers for a SOC of 0% and a temperature T of 25 °C.

Layer	Density ρ [kg m^{-3}]	Specific heat capacity c_p [J kg^{-1} K^{-1}]	Thermal conductivity parallel $\lambda_{\parallel}$ [W m^{-1} K^{-1}]	Thermal conductivity perpendicular $\lambda_{\perp}$ [W m^{-1} K^{-1}]
Anode current collector	8710[a]	385[a]	399[22]	
Cathode current collector	2707[a]	898[a]	236[22]	
Anode coating	1851[b]	955[b]	2.820[23]	
Cathode coating	2780[b]	784[b]	1.101[23]	
Separator	1139[b]	1700[b]	0.210[25]	
Housing	2660[a]	880[a]	108[a]	
Active material	2094[b]	1010[b]	1.741[b]	0.683[b]
Fully homogenized material	2894[b]	790[b]	69.904[b]	0.868[b]

[a]Experimentally determined; [b]Calculated according to Equation (4)–(7).

Figure 3. PH geometry with 8 unit cells and homogenized active material (light blue) layers. The other materials are colored in the same way as in Figure 1 and 2.

SOC of 0% and a temperature of 25 °C. The thermal transport properties of the anode and cathode current collectors are based on own experimental measurements for the density and heat capacity as well as literature data from Touloukian et al.[22] for the thermal conductivity. In contrast to this, the thermal parameters of the cell housing are determined completely in own experiments. In the case of anode and cathode coatings, the electrolyte phase is already included. The average density and specific heat capacity were calculated by classical phase-mixing laws weighted by the volume fractions v_i and the thermal bulk properties of the solid phase and electrolyte phase following the approach of Loges et al.[17] In contrast to the density and specific heat capacity, the determination of the effective thermal conductivity of electrode coatings is more complicated. Therefore, Oehler et al.[23,24] provide the values for the soaked electrode coatings, in which they developed a new concept for modeling the effective thermal conductivity of the coatings in the presence of an electrolyte phase. The density and specific heat capacity of the electrolyte-soaked separator layer have been calculated analogously to the electrode coatings with the mixing law. The effective thermal conductivity for the separator was taken from the contribution of Richter et al.[25]

In a last step, as explained in Section 2.2, different layers are homogenized. Therefore, it is necessary to calculate their effective density, effective specific heat capacity as well as the effective thermal conductivity in parallel $\lambda_{\mathrm{eff},\parallel}$ and perpendicular $\lambda_{\mathrm{eff},\perp}$ direction. The homogenized active material consists of the soaked anode and cathode coating as well as the soaked separator. The FH material in turn, in addition, contains the anode and cathode current collector foils. The calculations are performed according to Equation (6)–(9).[17]

$$\rho_{\mathrm{eff}} = \frac{\sum_i \rho_i v_i}{\sum_i v_i} \tag{6}$$

$$c_{\mathrm{p,eff}} = \frac{\sum_i \rho_i c_{\mathrm{p},i} v_i}{\sum_i \rho_i v_i} \tag{7}$$

$$\lambda_{\mathrm{eff},\perp} = \frac{\sum_i v_i}{\sum_i \frac{v_i}{\lambda_i}} \tag{8}$$

$$\lambda_{\mathrm{eff},\parallel} = \frac{\sum_i \lambda_i \cdot v_i}{\sum_i v_i} \tag{9}$$

i = anode coating; separator; cathode coating (active material)
i = anode current collector; anode coating; separator; cathode coating; anode current collector (FH)

3. Results and Discussion

A simulation without heat release serves as a baseline and for verification. All PH cases, the FH and FR cases with one-sided cooling are used for this (cf. Table 1). The point probes (A) and (B), marked in **Figure 4**, are chosen for the comparison. They are located in the yz-plane, in the cell center in x-direction, on the centerline in z-direction on the lower side (A) and upper side (B) of the cell stack. Thus, the points closest and furthest to the heat-sink boundary condition are selected.

Subsequently, the results of six different LoH are compared to the reference case presented by the FR geometry. For these, two additional dimensionless temperature point probes in the same yz-plane on the edge (C) and in the center (D) are plotted for a full discharge cycle. Both points are at a current collector sheet, except for the FH case clearly. The center point is generally of high relevance because of its long transport paths to the surfaces where the heat-sink boundary conditions are applied. Between this heat-sink boundary condition and the edge point (C) are only the outer separator and pouch foil. The effects of the LoH are first evaluated for one-sided cooling (1). 2D plots are shown for one PH case (ii) and compared to the FH (i) and FR (iii) cases in the same plane as the point probes above. Consequently, the results are compared for different cooling scenarios. Finally, the number of mesh elements and computing times for different cooling scenarios and LoH are compared.

To assess the dimensionless temperature correctly, the difference between the maximum and minimum temperature is necessary. In these simulation studies, the maximum temperature T_{max} occurs in the center of the cell stack in case of tab cooling for PH5. The minimum temperature T_{min} of 288 K is the heat-sink boundary condition, which corresponds to the dimensionless temperature of zero. Thus, differences in temperature can be compared with the maximum temperature difference ΔT_{max} of approximately 26.5 K. The other way around, the dimensionless temperature corresponds to an absolute temperature and can therefore be interpreted quantitatively. The initial dimensionless temperature is 0.378. The total heat-generation rate of the cell is 3 W, which corresponds to an average heat-generation rate at a 3C discharge. The dimensionless temperatures are plotted over the SOC, as an entire discharge at the predescribed conditions is simulated.

3.1. Heat Transport Paths

First, the results of pure thermal conduction, without heat generation, are shown. In a second step, the heat transport paths are discussed for a case with heat generation. A simulation study without heat-generation rate is performed on the scenario of one-sided cooling, which is shown in **Figure 5**. It has to be
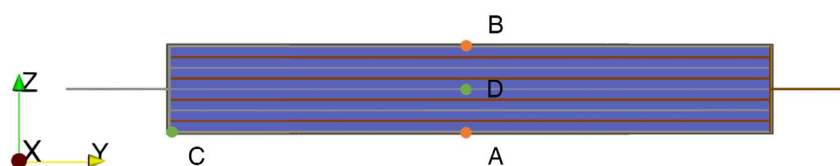

Figure 4. Evaluated point probes in the 2D yz-plane of the battery cell: (D) central, (C) edge, (A) lower side, (B) upper side.

ADVANCED
SCIENCE NEWS
www.advancedsciencenews.com

Energy Technology
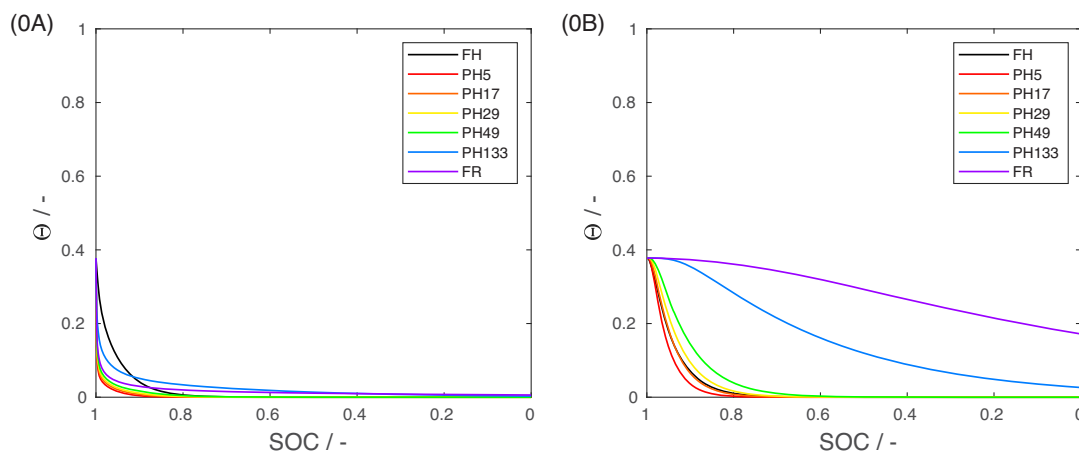Generation, Conversion, Storage, Distribution
www.entechnol.de

Figure 5. Temperature at the lower (A) and upper (B) point probe of the cell stack in case of one-sided cooling without heat release (0).

mentioned that without heat generation, SOC is not changing. Therefore, the cases without heat generation are simulated for the same time as those with applied discharge current. Then SOC is assigned according to the timeline during the discharge cycle to ease a comparison.

At the bottom of the cell stack (A), the temperatures follow an exponential decay. In all cases, the temperature declines to the dimensionless temperature of zero, which represents the temperature of the heat-sink boundary condition, at steady-state. The decline of the temperatures at the upper side of the stack (B) is a lot smaller than for the lower side (A). For the FR and PH133 case, the steady-state temperature is not yet reached at the end of discharge at the upper side of the stack (B). The gradient at the end of discharge implies that the temperature of the heat-sink boundary condition would be reached for a longer duration of the discharge. As point (B) takes the longest time due to the longest thermal transport path, all points in the geometry will eventually reach the heat-sink boundary condition temperature. The results are plausible on one hand, however, they indicate a strong impact of the LoH even in this relatively simple case. Both, qualitative as well as quantitative behavior varies to a great extent. This motivates a more detailed analysis, as it will follow in the next sections.

Now, the heat transport paths are discussed with heat generation for the different LoH at the four presented points in the cell stack in case of one-sided cooling (**Figure 6**).

In case of one-sided cooling (1) at the edge point (C), the temperatures instantly decay exponentially until all cases except for FR and PH 133 reach steady-state. The temperature at the end of discharge in case of FH is overestimated by 0.045 in comparison with FR. Interestingly, at the end of discharge and in the transient state, the PH cases underestimate the temperature in the order of their LoH. In comparison with the edge point (C), the temperatures at the end of discharge at the bottom (A) of the PH and FR cases are lower and they behave differently. Here, all PH cases seem to reach the same steady-state temperature. In case of FR, the temperature declines much more rapidly at the bottom (A) than at the edge (C), resulting in a lower steady-state temperature than the PH cases. In case of the FH case, the overestimation of the temperature is more pronounced at the

bottom (A) than at the edge (C). At the bottom (A), the steady-state temperatures of the PH reach a slightly lower level than at the edge (C).

In the center (D) of the cell stack, the temperatures in all cases do not drop right from the start. In contrast, they rise for a short period. After a small peak, they decrease more slowly than at the edge (C). All LoH, underestimate the temperature compared to the reference case (FR), in which it declines slowest of all cases. PH133 is closest to the FR case and has a similar decline, but still underestimates the temperature at maximum by 0.075. For the PH133 and FR case, the steady-state temperature is not yet reached at the end of discharge, but they will most likely decline to a similar steady-state temperature as the other PH cases. Interestingly, the temperatures of the PH cases at steady-state increase with greater homogenization, whereas the opposite applies during the transient state. This behavior can be seen more clearly at the top (B). The crossing occurs at a SOC of approximately 70%. Once more, the steady-state temperature of the FH case is higher than that of the other cases. Again, at the top of the stack (B), the temperatures are shifted upward. In addition, the peaks at the beginning are more pronounced and it takes longer until the curves are starting to decrease.

The direct decay at the lower side (A) and on the edge (C) can be explained by the short distance to the heat-sink boundary condition. For the FR and PH cases, the steady-state temperature on the edge (C) is higher than at the lower side (A), because the heat from other layers is distributed through the well-conducting tab T-junction. Consequentially, the heat is transported from the edge (C) through the lowest current collector layer to the bottom (A), which leads to a lower steady-state temperature at the edge for thicker current collector layers, such as PH5 in comparison with the other PH cases. The temperature at the end of discharge at the lower side (A) is lowest for the FR case. The only difference in the FR case to the PH133 case is the thermally poorly conducting separator. It inhibits thermal transport to the lower side in perpendicular direction through the cell stack. The FH case behaves very differently. It is the only case, where point (A) and (C) are not located on a highly conducting current collector, which directly contacts the separator shell layer and pouch foil.
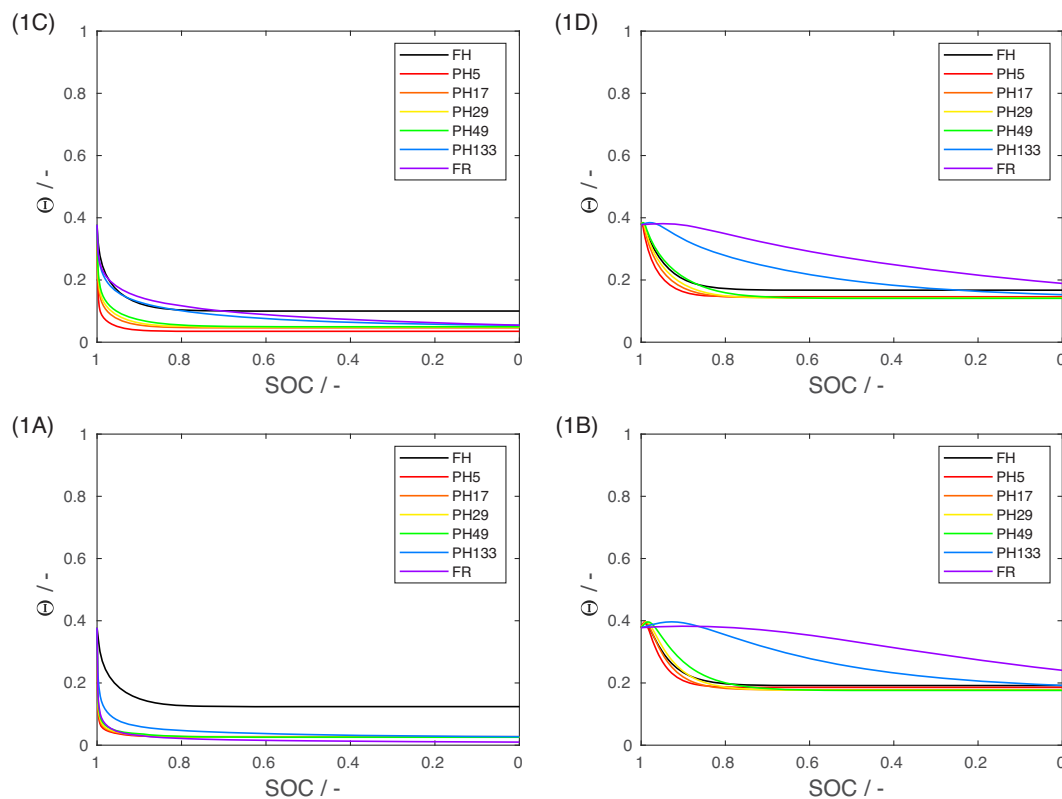
Figure 6. Temperature over SOC at edge (C), center (D), lower side (A) and upper side (B) point of the cell stack for one-sided cooling (1) for all LoH.

This fact results in a higher thermal gradient from the boundary condition to the point probes (A) and (C) in steady-state due to the lower effective thermal conductivity. This temperature is slightly higher on the lower side than on the edge, which might be due to the influence of the tab, which also has a short transport path to the heat-sink boundary condition at the edge. It is highly conducting and is connected to the point (C) from one side.

In contrast to the points close to the heat-sink boundary condition, there is a delay until the drop of the temperature in the center (D), which is caused by the significantly longer transport path. There even is a short increase due to the heat release. Clearly, the build-up of sufficient gradients is required first. This is exaggerated at the top (B), because it is even further away from the heat-sink boundary condition. The order of the curves of PH during the peak and the decrease in the temperature can be attributed to the order of the thickness of the current collectors, as only the current collectors are connected to the tab. The higher the LoH, the thicker the current collectors are, therefore the higher are the cross-sectional area to the tabs and the heat conduction. The described crossing of the temperatures at a SOC of approximately 70% shows that the thicker active material layers result in a higher thermal gradient in steady-state. The FH case again behaves differently than the others. The exponential decline at the beginning is steeper or equivalent in all the regarded points, but the steady-state temperature is higher. It seems that there are two different time scales. First, the conduction in z-axis is prominent, which results in a steep decline for the FH case caused by its higher cross-plane thermal conductivity

(cf. Table 2). In the long run though, the influence of the resolved tabs with high thermal conductivity in the other cases leads to higher heat transfer than in the FH. This heat transport path over the current collectors in y-axis and the bypass over the tab T-junction results in a time lag.

It is clear, that in case of one-sided cooling, there is a combination of thermal conduction in y- and z-direction. None of the homogenized cases can represent this combination of thermal conduction accurately. Especially the comparison with the FH case shows that the homogenization of the stack leads to a very different thermal conduction in y- and z-axis for a FH block with a resolved tab. Particularly, the temperature field at steady-state is much more homogeneous and the time until steady-state is very short at all regarded point probes. The homogeneous temperature field can be seen more clearly in **Figure 7**, which shows the 2D temperature plots in yz-plane of this scenario for FH (i1), PH133 (ii1), and FR (iii1) at SOC 80%. The PH133 case is shown, because of its best accordance with those of the FR case.

The temperature field of the cell stack of the FH case is already almost homogeneous. In contrast, the PH133 and the FR case depict a much higher temperature gradient along the z-axis with FR having the highest temperature gradient. In y-direction, the temperature in the stack is increasing from the tab to the cell center. In all cases, the lowest layer can be seen in a close up. This is the pouch foil, which has a lower temperature because of its high conductivity and spatial proximity to the heat-sink boundary condition. The pouch foil creates a bypass around
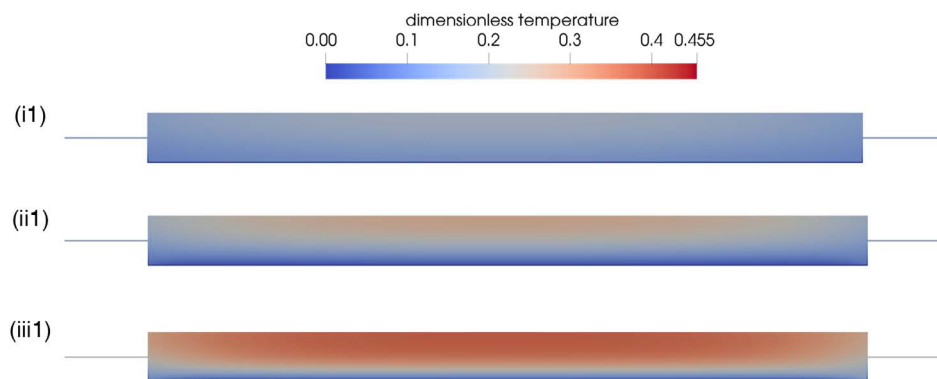
Figure 7. Temperature field at 80% SOC for FH (i), PH133 (ii), and FR (iii) cases and one-sided cooling (1).
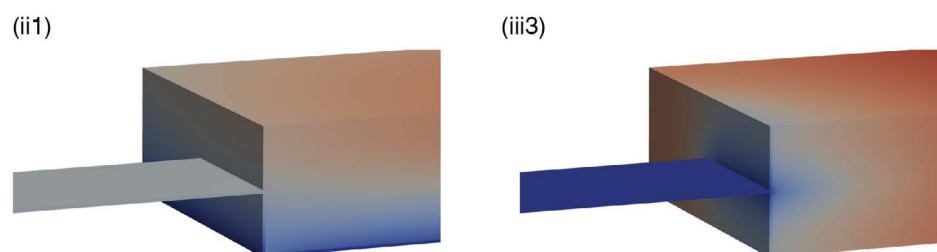

Figure 8. Magnification of a 3D temperature field at the cathode current collector and 80% SOC for the cases PH133 (ii) one-sided cooled (1) and (iii) tab cooled (3).

the cell in the direction of the horizontal part of the tab, which can be seen in detail in **Figure 8**. Due to the low conducting separator layer, enclosing the cell stack as well as the vertical part of the tab, the temperature is higher than in the pouch foil. The combination of this bypass and the low conducting layer results in a colder region close to the tabs. What can also be seen in Figure 8(ii1) is the negligible temperature gradient in x-direction. The temperature level of the FH case is already at 80% SOC much closer to steady-state. The homogeneous temperature distribution in the FH case points toward a different combination of thermal transport paths than for resolved current collectors (PH and FR). Clearly, the FH case does not display the internal temperature field accurately.

3.2. Cooling Scenarios

So far, the effects of the LoH are discussed for one cooling scenario. However, it is clear, that the internal temperature field is affected by a combination of heat transfer in y- and z-direction. Therefore, two-sided cooling and tab cooling are also regarded. It can be expected that two-sided cooling enhances the thermal transport in z-direction and tab cooling in y-direction.

When comparing the temperature plots of one-sided cooling (1) (Figure 6) and two-sided cooling (2) (cf. **Figure 9**), the shapes of the curves look quite similar. The difference in all plots is the steady-state temperature, which is closer to the heat-sink boundary condition for all the cases. When focusing on point (C), the steady-state temperature of FH is again overestimated. Similar to the transient behavior of the one-sided scenario, the decline is in

the order of the LoH. In the center (D), the same applies, but the differences to the FR case are a lot higher. Even the PH133, being closest to FR, has a maximum deviation of 0.168.

In comparison with one-sided cooling, the lower temperature level all over the cell is attributed to the twice as large heat-transfer area on both the opposite sides of the cell, resulting in significantly higher heat transport capability and thus a lower temperature level. The steady-state temperature of the FH case is slightly closer to that of the others for two-sided than for one-sided cooling. This points toward a more pronounced thermal transport in z-direction. This means that the impact of transport in y-direction over the bypass is lower, which is the reason that the steady-state temperature is not affected as much.

The lower temperature level can clearly be seen at 80% SOC in the 2D plots in **Figure 10**. The differences between the LoH are very clear. The temperature fields of FH and PH133 are almost homogeneous at a temperature close to the minimum temperature. The FR case on the other hand has a slightly higher temperature in the core of the cell stack. The FR case is still far away from steady-state at 80% SOC. The isotherm is elliptical. For these reasons, no PH case can reproduce the temperature field of FR.

The temperature plots (cf. Figure 9) for tab cooling (3) deviate from the others, in particular for the PH cases. At the edge (C), the temperatures decline immediately as already seen with one- and two-sided cooling, but the following behavior is very different. The temperature curves of the PH cases increase again after a minimum, which is most obvious in case of PH5 at a SOC of about 98.5%. It is noteworthy that PH133 has a slight incline in temperature at the end of discharge, the temperature of the FR
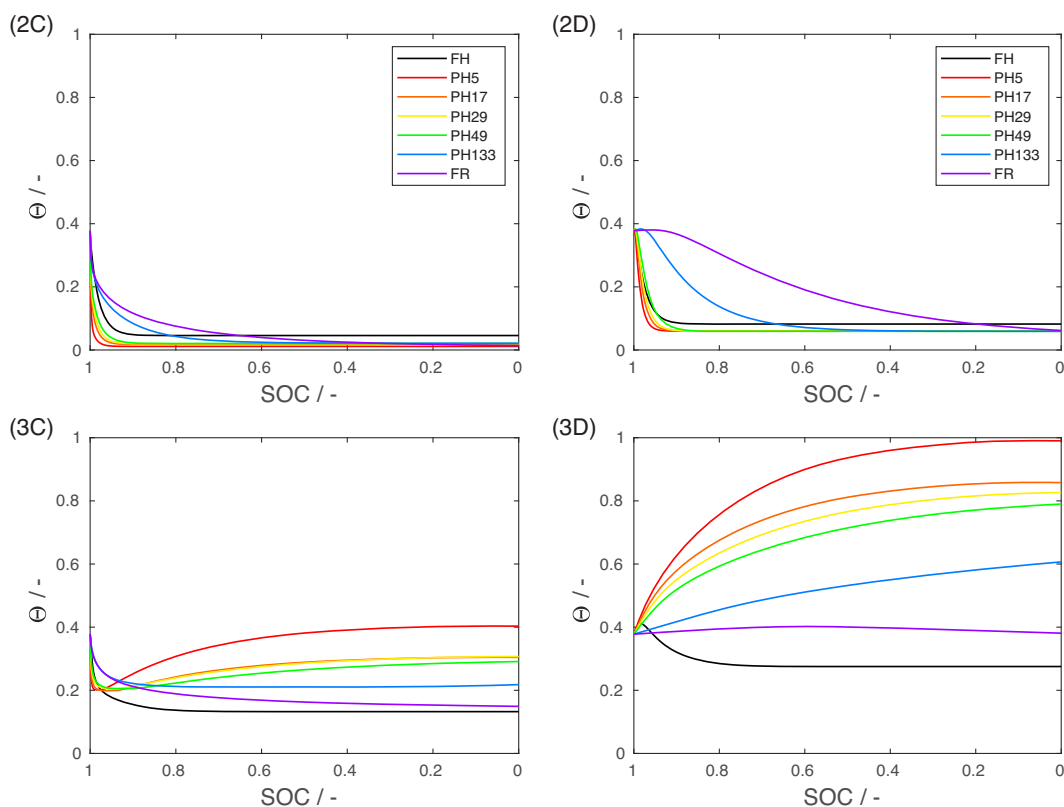
Figure 9. Temperature at edge (C) and center (D) point of the cell stack for two-sided (2) and tab cooling (3) for all LoH.
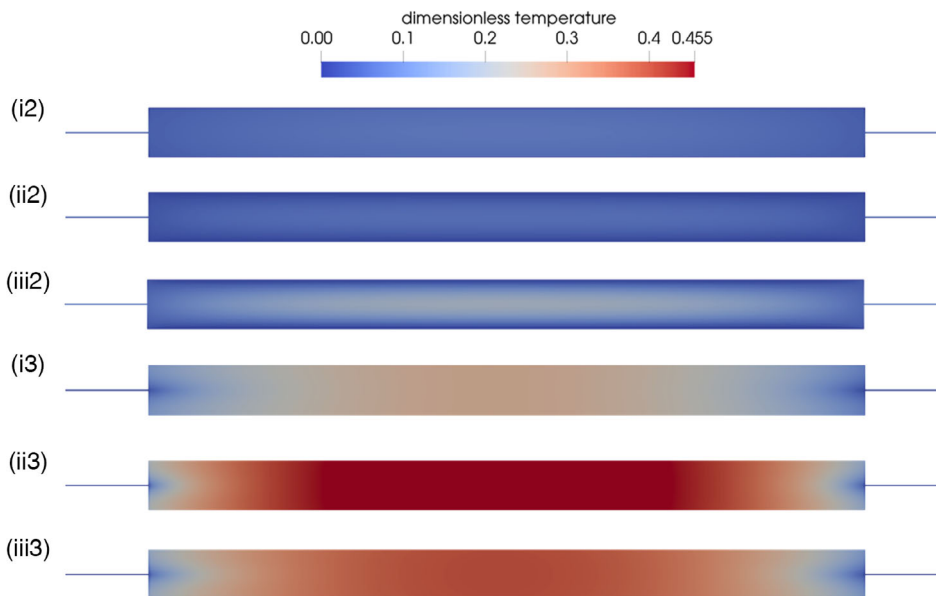

Figure 10. Temperature field at 80% SOC for FH (i), PH133 (ii), and FR (iii) cases and two-sided (2) and tab cooling (3).

case still declines and FH has already reached steady-state. Out of all cases, FH and PH133 come closest, but still over- and under-estimate the temperature of the FR case. In the center (D), the temperature in case of FR is almost constant at the initial temperature. There is only a minimal increase by less than 0.025 until SOC 60%, before it drops back to the initial temperature again. In all PH cases, the temperature increases continuously all over the entire discharge cycle, not achieving the steady-

ADVANCED
SCIENCE NEWS
www.advancedsciencenews.com

Energy Technology
Generation, Conversion, Storage, Distribution
www.entechnol.de

state temperature. They line up according to their LoH. The FH case on the other hand first peaks at SOC 95% and then declines to a steady-state below the temperature of FR.

At the edge (C), the heat is directly transported through the tab T-junction. Therefore, this leads to the drop in temperature. In the PH cases, after reaching the minimum, the temperature increases again due to a lag time until the temperature gradients are built from the active material layers to point (C). The temperature in case of FR continuously declines, which could be due to the thin coating layer close to point (C). Because the heat generation is distributed by the volumetric proportion of the active material, a thinner layer generates less heat in total. Again the temperature of FH shows a different behavior due to interaction of distribution of the heat release and the FH stack. Therefore, after reaching the minimum temperature, it does not increase again and the temperature is underestimated compared with FR. In the center (D), at the beginning of discharge in case of FH, there is heat generated in that particular point. In all other cases, the temperature gradients have to be built up from the active material to the highly conducting current collectors, which is directly connected to the tab. Therefore, the heat inlet and outlet is more equal for the FR and PH cases than for FH. The thickest active material layer again explains the highest temperature in the PH5 case. The less homogenized the geometry is, the smaller the layers are and the lower the temperature level is. The temperatures of PH133 and FH are closest to FR, but do not depict the temperature over discharge behavior accurately. The FH and FR cases show maxima in the center (D). Compared to the side-cooling scenarios, their maxima are at significantly lower SOC. Meaning, that the lag time until temperature gradients are developed is long. Possibly, even in the PH cases, a maximum could appear, if the discharge cycle lasted longer. The reasons for this huge time delay are the thin tabs resulting in a small cross-section area for thermal transport, the reduction of the transport path to almost exclusively y-direction as well as the much smaller heat-transfer area in the tabs in contrast to the side-cooling scenarios. Zhao et al.[5] already noticed, that the thermal transport from the current collectors to the tab is a bottleneck.

The 2D plots (cf. Figure 10(i3)–(iii3)) qualitatively have the same shape of temperature field for all LoH. The temperature level increases most for the PH case, less for FR, and least for FH for the same reasons as discussed in the last paragraph. Compared with the side-cooling cases, the temperature distribution is different. There is a cooler region close to the tabs, which reaches elliptically into the center. This elliptical temperature region can also be seen in the 3D plot in Figure 8(ii3). Clearly, the temperature gradient in x-direction is much more prominent than for one-sided cooling in Figure 8(iii3). However, the gradients in y- and z-direction have a greater relevance comparing the different cooling scenarios, so they are not discussed in this article in detail. This colder region is a little bit bigger for the anode than for the cathode tab. When taking a closer look at the colder region of PH133 and FR (cf. Figure 8(iii3)), the colder current collectors can be seen. Therefore, the lower temperature is caused by higher thermal conductivity of the copper anode current collector and anode tab compared with the aluminum cathode current collector and cathode tab.

With regard to the influence of the cooling strategies, the results generally agree well with results from literature.[5] One-sided cooling results in a temperature gradient over the z-axis. With two-sided cooling in turn, the steady-state temperature is close to the heat-sink boundary condition temperature. This intensifies, when applying a realistic cooling condition. The temperature field is most homogeneous over the whole discharge for tab cooling, which can be seen in Figure 9 and 10, respectively, with regard to the FR cases.

It is clear that the thermal conduction is highly affected by the interaction of the current collectors and the tab T-junction and the pouch foil, which cannot be replicated by a homogenized block. This marks a significant difference between this work and the work of Chen et al.,[14] where they did not resolve the tab and found, that a homogenized stack shows a sufficient accuracy.

3.3. Computing Time

When choosing an adequate LoH for an application, next to the accuracy of the calculations, the computing time is the other important criterion. The computing time depends on many factors, for example, the grid resolution and the amount of processors. The battery geometry with the applied boundary conditions is symmetric. In each cooling scenario, symmetry in yz-plane is used. For the two-sided and tab cooling, additionally the symmetry in xy-plane is exploited. The number of mesh elements used for some selected cases with one-sided cooling is given in **Table 3**. The correlation between the necessary fineness of the grid and the small size of the layers in the FR case is clearly reflected in a high computing time. All the cases are calculated in parallel using 32 processors of the BWUniCluster.[26]

Homogenizing the active material, leading to PH133, halves the number of mesh elements and the computing time in comparison with the FR case with 33.57 h. This applies similarly to a further homogenization from PH133 to PH49. FH only takes approximately 1.63 h. Using the additional symmetry of the xy-plane in case of two-sided and tab cooling reduces the computing time by about 60%.

With the prediction quality of the temperatures and the necessary computing time in mind, an optimal homogenization strategy can be chosen. Although none of the LoH can depict the FR case precisely, the PH133 case comes closest. This case has a significant reduction in computing time and can be of interest depending on the application. A further homogenization can be applicable, if a short computing time is of relevance. The deviation from the FR case can be predicted according to the results from Section 3.1 and 3.2.

Table 3. Number of degrees of freedom and computing time of selected cases.

Case	FR	PH133	PH49	FH
Number of mesh elements	22 295 420	9 200 868	3 044 820	669 744
Computing time [h]	33.57	16.80	7.64	1.63

**ADVANCED
SCIENCE NEWS**

www.advancedsciencenews.com

Energy Technology
Generation, Conversion, Storage, Distribution

www.entechnol.de

4. Conclusion

With these simulation studies, we have investigated the influence of different LoH of the cell stack on the internal temperature field. It has been shown that the FH cell stack with its homogenized, but still anisotropic thermal conductivity cannot replace a complex geometry consisting of multiple layers of very different thermal conductivities, even though the homogenization is being done according to the state of the art and reflects the conductivity, the density, and the heat capacity of all involved materials including its spatial distribution. First, the FH cases do not depict the thermal transport precisely, as clearly in the case of Li-ion batteries, the strong deviation of the bulk properties, specifically of the thermal conductivities of the different layers, limits applicability of the established methods. Second, a FR geometry offers different transport paths than a homogenized geometry, beyond the cell stack itself, such as current collectors, the separator layer wound around the stack as well as the pouch foil, including an aluminum layer.

Different cooling strategies also exploit different transport paths. The homogenization affects the temperature field of these different thermal scenarios with varying severity. For example, with tab cooling the critical thermal transport path is from the active material through the current collector layers to the tab. As PH increases the thickness of the homogenized active material layer, the center of the cell block is hotter than for the FR cases, as the transport path here perpendicular to the main transport direction is elongated. This is not physically reflected in the commonly used homogenization methodology. Only a FR geometry can depict the transient temperature distribution accurately. A reason for that seems to be the influence of the separator, with its specifically low thermal conductivity, in combination with the complex transport paths and cooling scenarios mentioned earlier. The same conclusion can be drawn for two-sided cooling but for a different reason. Two-sided cooling induces a very high temperature gradient across the stack. This aggravates the effect of the amount of layers and its thermal transport in z-direction. With one-sided cooling, there is a strong combination of thermal transport in y- and in z-direction and therefore two different time scales can be seen. In general, the case PH133 with a homogenized active material has the best accordance and can halve the computing time, but still does not depict the behavior accurately. The results show already, that a general methodology on how to do a proper homogenization of a pouched Li-ion battery cell cannot be proposed yet. It becomes clear, that the conventional approach does not reliably work, as soon as design elements such as current collectors, pouch foil, etc., are included in a model. This situation is further complicated by the influence of different cooling strategies. We continue our investigation to present a more generally applicable approach for the specific case of Li-ion cells, as the advantages of computing time reduction are clear.

[1] D. Werner, S. Paarmann, A. Wiebelt, T. Wetzel, *Batteries* **2020**, *6*, 13.
[2] D. Werner, S. Paarmann, A. Wiebelt, T. Wetzel, *Batteries* **2020**, *6*, 12.
[3] T. M. Bandhauer, S. Garimella, T. F. Fuller, *J. Electrochem. Soc.* **2011**, *158*, R1.
[4] D. Bernardi, E. Pawlikowski, J. Newman, *J. Electrochem. Soc.* **1985**, *132*, 5.
[5] Y. Zhao, Y. Patel, T. Zhang, G. J. Offer, *J. Electrochem. Soc.* **2018**, *165*, A3169.
[6] I. A. Hunt, Y. Zhao, Y. Patel, J. Offer, *J. Electrochem. Soc.* **2016**, *163*, A1846.
[7] R. Korthauer, *Lithium-Ion Batteries: Basics and Applications*, Springer, Berlin, Heidelberg **2018**.
[8] T. Hettesheimer, A. Thielmann, C. Neef, K.-C. Möller, M. Wolter, V. Lorentz, M. Gepp, M. Wenger, T. Prill, J. Zausch, P. Kitzler, *Entwicklungsperspektiven für Zellformate von Lithium-Ionen-Batterien in der Elektromobilität*, Fraunhofer-Institut für System-und Innovationsforschung ISI, Karlsruhe, Germany **2017**.
[9] G. Liebig, U. Kirstein, S. Geißendörfer, F. Schuldt, C. Agert, *Batteries* **2020**, *6*, 3.
[10] G. Guo, B. Long, B. Cheng, S. Zhou, P. Xu, B. Cao, *J. Power Sources* **2010**, *195*, 2393.
[11] Z. Li, J. Zhang, B. Wu, J. Huang, Z. Nie, Y. Sun, F. An, N. Wu, *J. Power Sources* **2013**, *241*, 536.
[12] J. Fleming, T. Amietszajew, J. Charmet, A. J. Roberts, D. Greenwood, R. Bhagat, *J. Energy Storage* **2019**, *22*, 36.
[13] X. Cui, J. Zeng, H. Zhang, J. Yang, J. Qiao, J. Li, W. Li, *Int. J. Energy Res.* **2020**, *44*, 3640.
[14] S. C. Chen, C. C. Wan, Y. Y. Wang, *J. Power Sources* **2005**, *140*, 111.
[15] S. Goutam, A. Nikolian, J. Jaguemont, J. Smekens, N. Omar, P. van Dan Bossche, J. van Mierlo, *Appl. Therm. Eng.* **2017**, *126*, 796.
[16] M. J. Hunt, F. Brosa Planella, F. Theil, W. D. Widanage, *J. Eng. Math.* **2020**, *122*, 31.
[17] A. Loges, S. Herberger, D. Werner, T. Wetzel, *J. Power Sources* **2016**, *325*, 104.
[18] W. Mei, Q. Duan, C. Zhao, W. Lu, J. Sun, Q. Wang, *Int. J. Heat Mass Transfer* **2020**, *148*, 119082.
[19] S. Allu, S. Kalnaus, W. Elwasif, S. Simunovic, J. A. Turner, S. Pannala, *J. Power Sources* **2014**, *246*, 876.
[20] F. Moukalled, L. Mangani, M. Darwish, *The Finite Volume Method in Computational Fluid Dynamics*, Springer International Publishing, Cham **2016**.

[21] A. Loges, S. Herberger, P. Seegert, T. Wetzel, *J. Power Sources* **2016**, *336*, 341.

[22] *Thermophysical Properties of Matter*, Vol. *1* (Ed: Y. S. Touloukian), IFI, New York, NY **1978**.

[23] D. Oehler, P. Seegert, T. Wetzel, *Energy Technol.* **2020**, *58*, 2000574.

[24] D. Oehler, J. Bender, P. Seegert, T. Wetzel, *Energy Technol.* **2020**, 2000722.

[25] F. Richter, S. Kjelstrup, P. J. S. Vie, O. S. Burheim, *J. Power Sources* **2017**, *359*, 592.

[26] BwUniCluster 2.0, https://wiki.bwhpc.de/e/Category:BwUniCluster_2.0 (accessed: October 2020).